nature energy

Article

https://doi.org/10.1038/s41560-025-01716-w

Asymmetric ether solvents for high-rate lithium metal batteries

Received: 22 August 2024

Accepted: 13 January 2025

Published online: 14 February 2025

Check for updates

Il Rok Choi[1,2], Yuelang Chen[2,3], Aditya Shah[2], Jacob Florian[2], Chad Serrao[1], John Holoubek[1,2], Hao Lyu[2], Elizabeth Zhang[1,2], Jun Ho Lee[1], Yangju Lin[2,4], Sang Cheol Kim[1], Hyunchang Park[2], Pu Zhang[1], Junyoung Lee[1], Jian Qin[2] ✉, Yi Cui[1,5,6] ✉ & Zhenan Bao[2] ✉

Recent electrolyte solvent design based on weakening lithium-ion solvation have shown promise in enhancing cycling performance of Li-metal batteries. However, they often face slow redox kinetics and poor cycling reversibility at high rate. Here we report using asymmetric solvent molecules substantially accelerates Li redox kinetics. Asymmetric ethers (1-ethoxy-2-methoxyethane, 1-methoxy-2-propoxyethane) showed higher exchange current densities and enhanced high-rate Li^0 plating/stripping reversibility compared to symmetric ethers. Adjusting fluorination levels further improved oxidative stability and Li^0 reversibility. The asymmetric 1-(2,2,2-trifluoro)-ethoxy-2-methoxyethane, with 2 M lithium bis(fluorosulfonyl)imide, exhibited high exchange current density, oxidative stability, compact solid–electrolyte interphase (~10 nm). This electrolyte exhibited superior performance among state-of-the-art electrolytes, enabling over 220 cycles in high-rate Li (50 µm)||$LiNi_{0.8}Mn_{0.1}Co_{0.1}O_2$ (NMC811, 4.9 mAh cm^{-2}) cells and for the first time over 600 cycles in anode-free Cu | |Ni95 pouch cells (200 mAh) under electric vertical take-off and landing cycling protocols. Our findings on asymmetric molecular design strategy points to a new pathway towards achieving fast redox kinetics for high-power Li-metal batteries.

Lithium-metal batteries (LMBs) have been investigated as promising candidates for advanced energy storage solutions and are actively being pursued for commercialization[1,2]. Despite much progress, LMB cycling performance remains limited due to the highly reductive environment near Li^0 and subsequent formation of unstable solid–electrolyte interphase (SEI)[3]. SEI cracking and dissolution are main factors attributing to continuous electrolyte decomposition and Li corrosion[4,5]. Moreover, uneven deposition of Li during charging promotes mossy Li growth, formation of inactive dead Li and eventual battery failure[6]. Numerous strategies for electrolyte design have been attempted to mitigate the above issues. Development of electrolyte formulations has focused on high Li^0 compatibility with stable SEI formation, improved oxidative stability, while also facilitating fast ion conduction for practical usage[7,8]. Noteworthy approaches include high-concentration electrolyte (HCE)[9,10], localized high-concentration electrolyte (LHCE)[11,12], functional additives[13,14] and high-entropy electrolytes[15,16].

Among the various electrolyte design strategies, controlling the degree of solvent fluorination has emerged as a promising strategy to enhance SEI reliability and homogeneous Li growth (Supplementary Fig. 1)[17–22]. Weakening solvation strength through steric hindrance or changing chelation sites results in anion-derived inorganic-rich SEI and higher coulombic efficiency (CE)[23]. The introduction of fluorine atoms to non-fluorinated ether backbone was shown to improve oxidative stability and further enhanced Li^0 compatibility. However, fluoroethers

[1]Department of Materials Science and Engineering, Stanford University, Stanford, CA, USA. [2]Department of Chemical Engineering, Stanford University, Stanford, CA, USA. [3]Department of Chemistry, Stanford University, Stanford, CA, USA. [4]Department of Chemistry, University of Waterloo, Waterloo, Ontario, Canada. [5]Stanford Institute for Materials and Energy Sciences, SLAC National Accelerator Laboratory, Menlo Park, CA, USA. [6]Department of Energy Science and Engineering, Stanford University, Stanford, CA, USA. ✉e-mail: jianq@stanford.edu; yicui@stanford.edu; zbao@stanford.edu

typically exhibit sluggish ion transport due to weak coordination with Li^+, hindering their high-rate performance in LMBs.

For high-power applications of LMBs, high ionic conductivity and transference numbers are necessary[24,25]. However, the Li^+/Li redox kinetics also play a pivotal role in influencing rate performance[26]. Fast desolvation and high exchange current density are crucial for minimizing charge transfer resistance and preventing solvent decomposition and enabling high C-rate performance[27,28].

Here we report an asymmetric ether solvent design for high-rate LMBs, characterized by their fast redox kinetics. We found that 1-ethoxy-2-methoxyethane (EME) and 1-methoxy-2-propoxyethane (MPE), when paired with 1 M lithium bis(fluorosulfonyl)imide (LiFSI), exhibited higher exchange current density compared to symmetric ethers (1,2-dimethoxyethane (DME), DEE). They gave enhanced CE and reduced overpotential in high-rate Li | |Cu cells. Next, fluorination of EME improved oxidative stability and further enhanced reversibility of Li plating/stripping. Examination of different degrees of fluorination on the β-carbon of EME revealed that F3EME exhibited the highest oxidative stability and Li compatibility, yielding a compact and Li_2O-rich crystalline SEI (~ 10 nm thickness). Further comparison between asymmetric and symmetric fluorinated ethers confirmed faster charge transfer kinetics in asymmetric fluorinated ethers, resulting in improved high-rate performance. Specifically, F3EME electrolytes demonstrate >220 cycles in high-rate 50-µm Li | |4 mAh cm^{-2} NMC811 cells (2 mA cm^{-2} charge, 4 mA cm^{-2} discharge) and >350 cycles in 20 µm Li | |3 mAh cm^{-2} $LiFePO_4$ (LFP) full cells (1.5 mA cm^{-2} charge, 3 mA cm^{-2} discharge).

Finally, to assess the potential for high-rate LMBs, we applied a cycling protocol specifically designed for electric vertical take-off and landing (eVTOL) scenarios[29]. eVTOL operations necessitate batteries with high power density or C-rate during vertical ascents and descents (3 C for approximately 30 s each), along with high energy density for sustained cruising over longer distances. Our high-rate LMBs, enhanced by F3EME solvent, exhibited a promising potential for such applications, demonstrating >600 cycles in anode-free Cu | |Ni95 200 mAh pouch cells.

Design logic of asymmetric ether solvents

Ether structures have been widely used as electrolyte solvents for LMBs as they exhibit relatively higher stability against Li^0 compared to carbonates[30]. 1,2-dimethoxyethane (DME), a well-explored ether structure featuring an ethylene glycol moiety, has chelation with Li^+ in a stable five-membered ring configuration, facilitating efficient solvation and rapid ion diffusion. On the other hand, 1,2-diethoxy ethane (DEE) preserves the ethylene glycol framework but with weakened Li^+ solvation from steric hindrance. DEE as a solvent showed improved CE, albeit with poor charge/discharge rate capabilities[19].

Recognizing the pivotal roles of kinetic performance and ionic conductivity in achieving high-rate capabilities, this study proposes a novel molecular design strategy to enhance the above parameters. We found that solvents with asymmetric structures (MPE, EME; Fig. 1a) exhibited superior exchange current densities over their symmetric counterparts (DME, DEE) and enhanced CE under high-rate conditions. Recent work reported the use of an asymmetric solvent EME to improve compatibility with $LiPF_6$ salt for improved cycling of alloying anodes in Li-ion batteries[31]. Our study here focuses on charge transfer rate impacted by solvent molecular design and offers new insights into the mechanism of solvent asymmetry. Moreover, the fine tuning of solvation free energy and ionic conductivity led to the selection of EME for subsequent introduction of fluorine atoms.

Three fluorinated derivatives of EME were investigated (F*x*EME, $x = 1–3$; Fig. 1a). Notably, fluorination at the β-carbon has previously been reported to enhance both oxidation stability and anion-derived SEI formation[32]. This trend was also observed in F*x*EME series. Compared with the F*x*DEE family (Fig. 1a), F*x*EME series were found to consistently exhibit higher exchange current density (j_0) and ionic conductivity relative to F*x*DEE.

F3EME emerged as the top performer, demonstrating three distinct characteristics essential for high-rate LMBs (Fig. 1b). First, its asymmetric structure led to rapid Li redox kinetics as evidenced from its high exchange current density. Second, the EME backbone design gave reduced bulk impedance and stable SEI formation. Third, the electron-withdrawing nature of the -CF_3 group further improved the compact SEI formation and enhanced oxidative stability enabling compatibility with high-voltage cathodes[32]. These attributes render F3EME suitable for applications requiring high power density, fast-charging capabilities and enhanced energy density, such as anode-free LMBs for eVTOL[29,33].

Comprehensive design principles underlying the EME and F*x*EME ($x = 1–3$) series are summarized in Supplementary Fig. 2, and detailed physico-chemical properties of developed solvents and electrolytes (1 M LiFSI in non-fluorinated ether series (DME, EME, MPE, DEE) and 2 M LiFSI in F*x*EME) are presented in Supplementary Tables 1 and 2.

Effect of solvent asymmetry on electrolyte properties and CE

The solvation free energy (ΔG_{solv}, referenced to 1 M LiFSI in DEC) was found to increase (weaker solvation) with an increased number of side carbons (DME: 2, EME: 3, MPE, DEE: 4). This trend has been previously attributed to the increased steric hindrance that weakens solvation strength (Fig. 2a and Supplementary Fig. 3)[19]. Raman spectroscopy showed a higher percentage of contact ion pairs (CIP) and aggregates (AGG) consistent with increased ΔG_{solv} (Fig. 2a and Supplementary Fig. 4)[9]. Molecular dynamics (MD) simulations supported these findings, showing increased Li^+-anion clusters (LAC) and reduced Li^+-solvent coordination in weaker solvating environments (Supplementary Fig. 5). Ionic conductivity measurements (with and without Celgard 2325 separator) revealed an inverse correlation with solvation free energy (Fig. 2a), suggesting that weaker solvation leads to increased ion clustering and reduced ion conduction, consistent with previous reports[20].

Exchange current density (j_0) measurements using ultra-microelectrodes ($D = 25$ µm) and transient cyclic voltammetry (scan rate = 100–200 V s^{-1}) revealed that asymmetric ethers (MPE, EME) exhibited substantially higher j_0 values and faster redox kinetics compared to the corresponding symmetric ethers (Fig. 2b and Supplementary Figs. 6 and 7). Notably, despite similar (or stronger) solvation strength between MPE (or EME) and DEE, asymmetric ethers showed higher j_0 than DEE. This contradicts the previously reported trend that weaker solvation of Li^+ lowered the electron transfer barrier, resulting in larger j_0[34,35]. Moreover, entropy change (ΔS), calculated from the temperature dependence of ΔG_{solv}, as reported previously[36], was higher in 1 M LiFSI in MPE than DEE, despite the same molecular weight and similar ΔG_{solv} at room temperature (Supplementary Fig. 8). The higher configurational entropy change of asymmetric MPE electrolyte might be due to a higher number of solvent molecules released after the desolvation process.

Next, the high-rate Li plating/ stripping reversibility was tested with Li | |Cu half cells cycled at different current densities (0.2, 0.5, and 2 mA cm^{-2}) and same areal capacities (1 mAh cm^{-2}) (Fig. 2c). Whereas DME, with strong solvation power, exhibited unstable CE throughout current density variations, EME, MPE and DEE electrolytes demonstrated stable CE (> 99.0%) at 0.2 mA cm^{-2}. At higher current densities, DEE required an extended activation cycle number (>20 cycles) to stabilize CE at 0.5 mA cm^{-2}, whereas asymmetric solvents (EME, MPE) achieved rapid activation (less than five cycles) and maintained higher CE than DEE, consistent with Aurbach CE measurements (MPE (99.13%) - EME (99.12 %) > DEE (98.85%), Supplementary Fig. 10)[37,38]. At high-rate cycling (2 mA cm^{-2}), EME showed the fastest activation followed by MPE, whereas DEE experienced issues with

https://doi.org/10.1038/s41560-025-01716-w

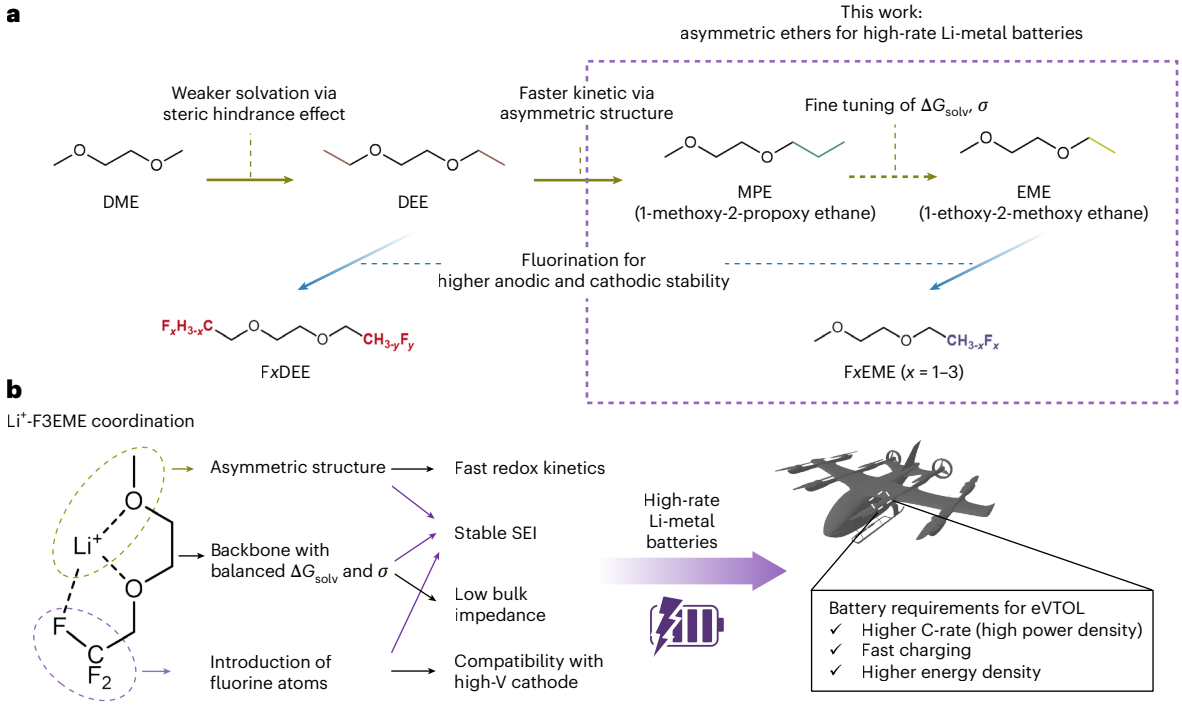

Fig. 1 | Design of asymmetric solvent molecule for high-rate performance Li-metal batteries. a, Step-by-step design principles of asymmetric ether solvent, from optimizing non-fluorinated ether skeleton to fluorinating with different degrees. **b**, Favourable characteristics of F3EME-based electrolyte towards high-rate Li-metal batteries and its practicability test with eVTOL protocol. Credit: **b**, eVTOL model, EveAir under a Creative Commons license CC BY 4.0.

soft shorting and slow CE activation (Fig. 2c and Supplementary Figs. 11 and 12).

The superior performance of MPE, despite similar ionic conductivity and ΔG_{solv} as DEE, was attributed to faster kinetics leading to favourable Li plating morphology, SEI formation and overall lower impedance. First, scanning electron microscopy (SEM) analysis of initial Li plating revealed more mossy morphologies with DEE under high-rate conditions compared to EME or MPE (Supplementary Fig. 13). X-ray photoelectron spectroscopy (XPS) analysis of residual SEI (rSEI) compositions (Fig. 2d and Supplementary Fig. 14) following 20 cycles at 2 mA cm^{-2} revealed higher concentrations of dead Li and lower oxygen or fluorine content in DEE electrolytes compared to EME or MPE. Moreover, asymmetric ethers showed a higher ratio of inorganic (N + F + S) to organic components (C) than DEE, which reflects the inorganic-rich SEI (Supplementary Fig. 15). This indicates that the faster kinetics in EME and MPE contribute to the efficient Li^+ reduction instead of solvent reduction, resulting in a more stable SEI formation and reduced dead Li accumulation[27,39,40]. Voltage profiles under high-rate conditions showed lower overpotential for asymmetric solvents (EME, MPE) compared to DEE (Fig. 2e). This difference can be attributed to several factors, including bulk impedance (R_{bulk}), SEI resistance (R_{SEI}) and charge transfer resistance (R_{ct})[41]. Galvanostatic electrochemical impedance spectroscopy (GEIS) data were measured after 20 cycles in Li | |Cu coin cells and the current density of 2 mA cm^{-2} was applied during the process of Li plating (Fig. 2f and Supplementary Fig. 16). The faster kinetics observed in asymmetric solvents appeared to lower all impedance factors (low R_{bulk}, R_{SEI} and R_{ct}), contributing to the lower overpotential. As asymmetric solvents provide faster redox kinetics (low R_{ct}), the low R_{SEI} may be due to less solvent decomposition forming a more inorganic-rich stable SEI. Although MPE and DEE have the same ionic conductivity, the lower R_{bulk} in MPE could be due to reduced electrolyte consumption during the cycling.

Despite the enhanced CE achieved using asymmetric solvents with higher j_0, their compatibility with high-voltage cathodes remains limited. This underscores the necessity for further investigations into fluorination strategies[32], particularly targeting EME due to its balanced properties of weak solvation and high ionic conductivity, alongside its superior exchange current density.

Effect of different fluorination levels in EME

We proceeded to fluorinate the β-carbon of EME to varying degrees (F*x*EME, $x = 1–3$). Initially, we optimized the concentration to achieve the highest ionic conductivity, using Celgard 2325 as the separator (Fig. 3a). The peak ionic conductivity was found to be 2 M for all solvents, which was selected for further analysis of electrolyte properties and electrochemical stability.

As expected, increasing the degree of fluorination corresponded to weaker coordination with Li^+, evidenced by higher ΔG_{solv} values, an increased (CIP + AGG) ratio and a higher LAC percentage in more fluorinated EME (Supplementary Figs. 3, 17 and 18). Furthermore, weaker solvation resulting from fluorination was accompanied by lower ionic conductivity and increased overpotential in Li || Li symmetric cells (Fig. 3a and Supplementary Fig. 19).

F3EME demonstrated the highest anodic stability at elevated voltages (Fig. 3b). The trend aligned with the fluorination level: F3EME > F2EME > F1EME > EME. Linear sweep voltammetry (LSV) on Li || Al and Li || Pt half cells further assessed corrosion of the Al current collector and the intrinsic oxidative stability of the electrolytes (Fig. 3c)[42]. Results generally mirrored those from Li || NMC811 CV tests, though 2 M LiFSI in F2EME exhibited distinct peaks (3.1, 3.5 V) in Li || Pt LSV, indicating its intrinsic instability at high voltage and potentially influencing subsequent NMC full-cell cycling outcomes.

Electrochemical stability at the Li-metal anode was evaluated across these four electrolytes. Aurbach coulombic efficiency (CE) measurements in Li || Cu half cells ranked the stability as F3EME > F2EME > EME > F1EME (Fig. 3d and Supplementary Fig. 20)[37]. The instability of F1EME may be attributed to slightly longer C–F bond length (density functional theory (DFT) calculated) which makes it

https://doi.org/10.1038/s41560-025-01716-w

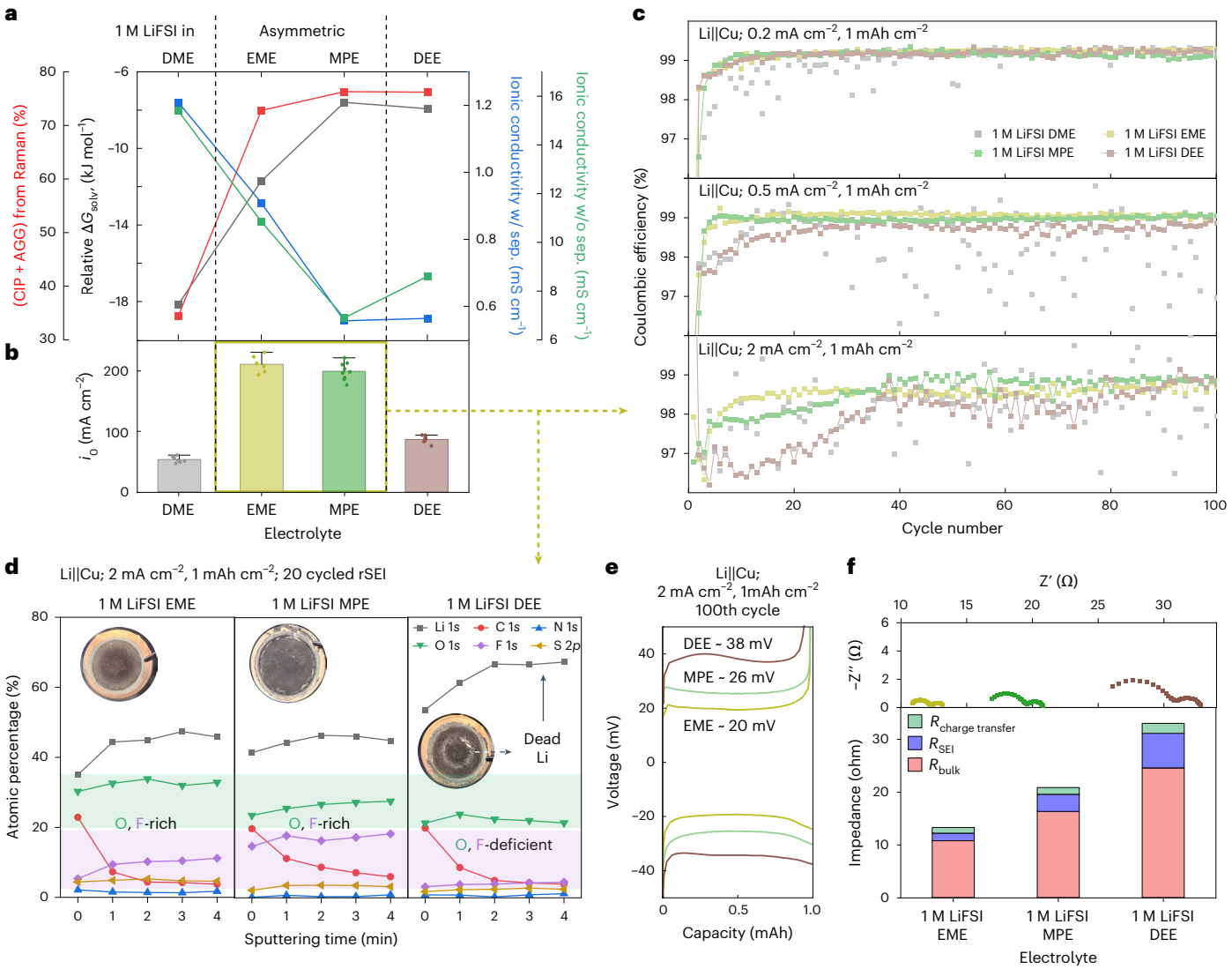

Fig. 2 | Effect of solvent asymmetry on lithium-metal compatibility–optimization of non-fluorinated backbone structure. a, Solvation strength analysed with relative solvation free energy (ΔG_{solv}) measurement[71] and Raman spectroscopy and its correlation to ionic conductivity of 1 M LiFSI in DME, EME, MPE, DEE (with (w/, blue) and without (w/o, green) Celgard 2325 separator (sep.), sample size $n = 4$). **b**, Exchange current density measured with ultra-micro electrode (UME). Details of measurement are shown in Supplementary Fig. 6 ($n = 6$ for EME, DEE and 9 for DME, MPE; each measurement performed with polished UME and separate transient voltammetry; data are presented as mean values ± standard deviation (SD)). **c**, Li || Cu half cells cycling with different current density (0.2, 0.5, 2 mA cm^{-2}) and same areal capacity (1 mAh cm^{-2}). Repeated cells are shown in Supplementary Fig. 9. **d**, XPS elemental analysis of rSEI after 20 cycled Li || Cu (2 mA cm^{-2}, 1 mAh cm^{-2}) using 1 M LiFSI in EME, MPE, DEE. Inset: images of rSEI on Cu. **e**, Voltage profiles at 100th cycle of Li || Cu cycled with 2 mA cm^{-2} current density for each electrolyte. **f**, Nyquist plots of galvanostatic electrochemical impedance spectroscopy (GEIS, 2 mA cm^{-2}) after 20 cycled Li || Cu (2 mA cm^{-2}, 1 mAh cm^{-2}) (up) and breakdown of impedance contribution (R_{bulk}, R_{SEI}, $R_{charge\ transfer}$) after deconvoluting the GEIS curves (down).

more reactive (Supplementary Fig. 21)[43]. Conventional Li || Cu long cycling tests (0.5 mA cm^{-2}, 1 mAh cm^{-2}) generally followed the Aurbach CE measurements trend (Fig. 3e). The best-performing 2 M LiFSI in F3EME electrolyte exhibited rapid activation within three cycles, reaching 99% CE and maintaining a low CE fluctuation of ±0.04% (Supplementary Fig. 22). In contrast, EME-based electrolytes showed substantial CE fluctuations after 200 cycles, indicating that fluorination improved Li plating/stripping reversibility by weakening solvation structures. SEM analysis of plated Li morphology showed chunkier deposits with F2EME and F3EME, while mossy growth occurred with F1EME electrolyte (Supplementary Fig. 23).

To investigate the effect of fluorination on SEI chemistry and its impact on CE, various techniques were employed to analyse residual SEI (rSEI) and direct SEI. XPS analysis of rSEI from 20 cycled Li || Cu cells indicated an increased (N + F + S)/C ratio for F3EME electrolytes, followed by EME > F2EME > F1EME (Fig. 3f brown line and Supplementary Figs. 24 and 25). A higher ratio of inorganic (N + F + S) to organic components (C) suggests an inorganic-rich SEI. Furthermore, H_2O titrations were performed with rSEI from 20 cycled Li || Cu to measure the amount of dead Li through quantifying produced H_2 gas with gas chromatography[44,45]. The dead Li amount decreased with increased (N + F + S)/C ratio, in the order of F3EME < EME < F2EME < F1EME (Fig. 3f grey line and Supplementary Fig. 26). These findings are consistent with previous reports, suggesting inorganic-rich SEI suppresses mossy or dead Li formation and is considered a favourable SEI[46]. Cryo-TEM of direct SEI further highlighted F3EME's distinctive feature, showing the most compact SEI with a thickness of approximately 10 nm (Fig. 3f bar graph and Supplementary Figs. 27 and 28)[47]. Remarkably, the compact SEI from F3EME was Li_2O-rich and crystalline with a grain size of ~1–2 nm (Fig. 3g and Supplementary Fig. 29). It was previously

https://doi.org/10.1038/s41560-025-01716-w

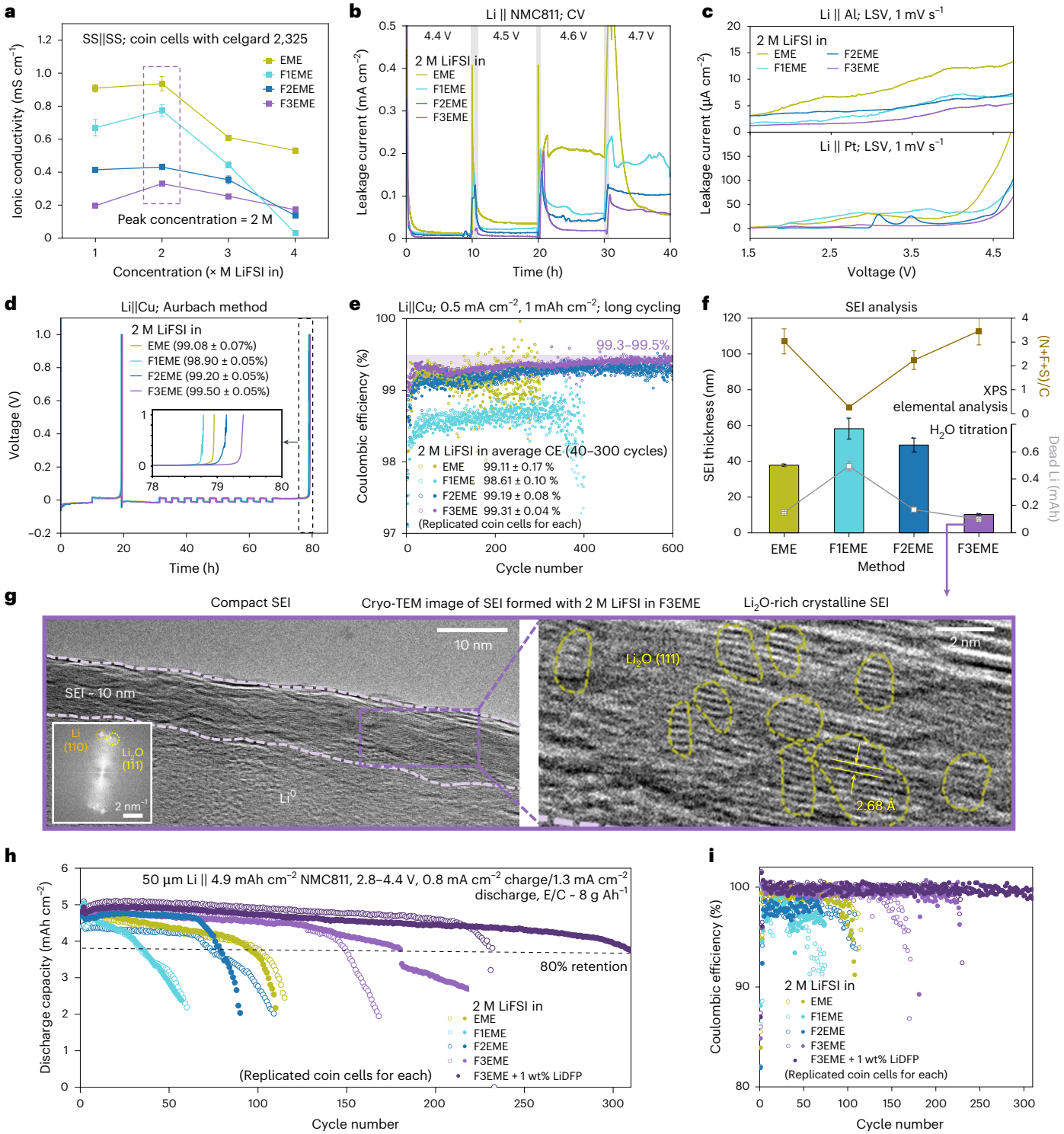

Fig. 3 | Investigation on the different degree of fluorination on EME. a, Ionic conductivity measurement in presence of Celgard 2325 separator with different concentrations of F*x*EME electrolytes (sample size $n = 4$; each measurement from different EIS curves; data are presented as mean values ± SD). **b**,**c**, Oxidative stability was measured with stepwise constant-voltage (CV) measurements using Li | |NMC811 full cells (**b**) and linear sweep voltammetry (LSV) measurements using Li | |Al and Li | |Pt (**c**). **d**, Aurbach method[37,38] in Li | |Cu half cells to calculate the average Li-metal CE (three repeated cells are shown in Supplementary Fig. 20). **e**, Li | |Cu long cycling performance at 0.5 mA cm^{-2} current density and 1 mAh cm^{-2} areal capacity. **f**, SEI analysis using various methods. (N + F + S)/C ratio was calculated with XPS elemental analysis (brown line, $n = 3$; each measurement from three spots on the same sample (20 cycled all stripped Cu surface); data are presented as mean values ± SD). The amount of inactive Li in rSEI was quantified with H_2O titration (grey line, $n = 3$; each measurement performed with cycled Cu in separate coin cells; data are presented as mean values ± SD). The thickness of direct SEI was measured with cryo-TEM (bar graph, $n = 2$; each measurement performed with different Li dendrites; data are presented as mean values ± SD). **g**, Cryo-TEM image of direct SEI formed with 2 M LiFSI in F3EME, demonstrating a compact SEI with 10 nm thick SEI (left, inset: FFT image of Supplementary Fig. 29a) and a Li_2O-rich crystalline SEI (right, d-spacing of 2.68 Å indicating a Li_2O (111) plane). **h**,**i**, 50 μm Li || 4.9 mAh cm^{-2} NMC811 full-cell long cycling performance (**h**) and CE (**i**). Conditions: 2.9–4.4 V, 0.8 mA cm^{-2} charge, 1.3 mA discharge cm^{-2}, electrolyte-to-capacity ratio (E/C) ~ 8 g Ah^{-1}. Note: replicated cell results are shown in **e**,**h**,**i**.

observed that Li_2O/Li interphase could reduce the diffusion barrier for Li^+[48]. The general trend of SEI thickness aligned with the previous XPS and titration results, indicating that forming a stable initial passivation layer effectively prevents subsequent side reactions between the electrolytes and the Li surface. Finally, focused ion beam-scanning electron microscope (FIB-SEM) analysis of rSEI indicated thinner rSEI in F2EME and F3EME compared to EME or F1EME, potentially influencing long-term Li || Cu cycling performance (Supplementary Fig. 30). The differences in SEI chemistry and structure across the four electrolytes were consistent with CE results, suggesting that the F3EME with weaker solvation and suitable molecular structure contributed to inorganic-rich, highly crystalline and compact SEI, which enhanced Li plating/stripping reversibility.

Following a comprehensive analysis of electrolyte properties and electrochemical stability in the F*x*EME series, we assessed Li-metal full-cell performance using thin Li foil (50-µm thick) paired with an industrially relevant high-loading NMC811 cathode (~4.9 mAh cm^{-2}). These coin cells were cycled at 0.8 mA cm^{-2} charge and 1.3 mA cm^{-2} discharge rates, with cycle life (80% capacity retention) ranking as F3EME > EME ~ F2EME > F1EME (Fig. 3h). Addition of 1 wt% LiDFP to the F3EME electrolyte further enhanced the cathode stability, probably forming a stable CEI with LiDFP decomposition (Supplementary Fig. 31)[14,49]. With LiDFP enhancement, the F3EME electrolyte maintained stable capacity over 300 cycles, positioning it among state-of-the-art electrolytes (Supplementary Table. 3). F3EME demonstrated high and stable full-cell CEs before failure and voltage polarization trends correlated with full-cell cyclability, indicating sharp increases in polarization upon substantial capacity loss (Fig. 3i and Supplementary Figs. 32 and 33)[50].

Effect of solvent asymmetry in fluoroether electrolytes

Next we conducted a comprehensive comparison between the asymmetric F*x*EME series and the F*x*DEE family[20], which was previously reported to give high CEs and good oxidative stability. Among the F*x*EME and F*x*DEE electrolytes, 2 M LiFSI in F2EME and F3EME were selected for their notably high Li || Cu CE (Fig. 3d,e). Similarly, 2 M LiFSI in F3DEE was chosen due to its structural similarity to F3EME (with concentration also set at 2 M for equitable comparison) and 1.2 M LiFSI in F4DEE and F5DEE were selected for their previously reported superior performance in full cells. Figure 4a shows the calculated coordination of Li^+ with each solvent. Compared to F4DEE and F5DEE, F3DEE-related solvation structure exhibited relatively greater asymmetry as seen by only one F-Li^+ coordination from one side instead of two F-Li^+ coordination from both sides.

The redox kinetics and ionic conductivity of each electrolyte are shown in Fig. 4b. We found that F3DEE showed faster kinetics compared to symmetric F4DEE and F5DEE. In addition, the asymmetric F*x*EMEs have higher exchange current densities despite stronger solvation compared to all F*x*DEEs (Supplementary Figs. 3 and 34). The ionic conductivity was also higher in F*x*EME than in F*x*DEE. Additionally, a higher degree of fluorination is known to lead to weaker solvation due to the inductive effect of fluorine atoms, resulting in lower ionic conductivity. The ionic conductivity trend mirrored that of solvation strength, ranking as follows: F2EME > F3EME > F3DEE > F4DEE > F5DEE.

Effect of redox kinetics on the high-rate LMB performance was evaluated by cycling tests of Li || Cu under three different high-rate conditions. With first condition (2 mA cm^{-2} plating/stripping of 1 mAh cm^{-2} Li), all electrolytes except F4DEE exhibited stable CE above 99% with delayed activation around 60 cycles (Fig. 4c). However, the cycle number at which substantial fluctuation began varied, ranking as F3EME ~ F2EME > F3DEE > F5DEE > F4DEE. This trend followed the exchange current density trend rather than solvation free energy trend. Similar trends were observed under the second condition (2 mA cm^{-2} plating / 4 mA cm^{-2} stripping of 4 mAh cm^{-2} Li; Fig. 4d). F4DEE and F5DEE showed large fluctuation from the first cycle whereas others showed stable CEs over 99.0%, where CE fluctuation started later in the trend of F3EME > F2EME > F3DEE. Despite slightly lower j_0, F3EME outperformed F2EME probably due to its SEI stability (Fig. 3f), suggesting that both weakly solvating structures for stable SEI and higher j_0 are critical for high-rate performance. Finally, for Li || Cu cycling at stepwise current densities (0.2–8 mA cm^{-2}, 1 mAh cm^{-2}), F3EME was the only electrolyte to maintain ~97.5% CE at 8 mA cm^{-2} with relatively lower overpotential (Fig. 4e and Supplementary Figs. 38). Li morphology supported these findings (Supplementary Figs. 39 and 40), showing that F*x*EME electrolytes exhibited chunkier and desired Li deposits compared to mossy Li observed with F*x*DEE, which correlated with their high-rate Li || Cu performance[51,52].

Lastly, since overpotential is another critical parameter in LMBs as it is directly related to the energy efficiency[53], we evaluated this parameter by cycling Li || Li symmetric cells under various current densities from 1 mA cm^{-2} to 10 mA cm^{-2} with an areal capacity of 3 mAh cm^{-2} (Fig. 4f). F4DEE and F5DEE started to show a large overpotential from 4 mA cm^{-2}. Other electrolytes showed more stable voltage profiles and the overpotential followed the trend of: F2EME < F3EME < F3DEE, which is inversely correlated with ionic conductivity.

Proposed mechanism of solvent asymmetry effect on higher j_0

Previous work has reported that weaker solvation was correlated with higher exchange current density (j_0)[35]. This trend is not as clear in our data (Supplementary Fig. 41), suggesting other factors need to be considered. In this section, we propose an approach to quantify solvent asymmetry and a mechanism explaining the enhancement of j_0.

First, using DFT, we estimated the dipole moments of systems containing one solvent molecule and one Li^+ (Supplementary Fig. 43). The dipoles of asymmetric solvents are seen to be 'tilted' towards their more electron-rich ethyl or propyl tails, whereas those of the symmetric solvents showed no such orientation. To quantify solvent asymmetry, we (1) projected the dipole (pointing from positive to negative) onto the best-fit plane containing the backbone of the solvent molecule and (2) found the acute angle between the projection and the normal to the line connecting the oxygen atoms in the solvent molecule (Supplementary Fig. 42). The larger the angle, the more asymmetric the molecule is considered. The strong positive correlation between this 'dipole orientation angle' and j_0 (Fig. 5c) suggests it has a connection with Li^+/Li redox kinetics.

It is well documented that the negative polarization of the anode surface during lithium plating influences the spatial distribution of solvents and ions. This causes anions to be repelled and for the molecules in the solvation shell around a Li^+ to reorient themselves as they approach the surface during the desolvation process[54,55]. As a result, anions would move to the far side of the solvation shell (relative to the surface), even if they are not removed from the solvation shell entirely. However, solvent molecules that remain in the close vicinity of the Li^+ and the anode surface will shield the Li^+ redox pathway, and its rate of de-shielding will impact charge transfer rate.

Under an electric field, dipoles align parallel to the field. We hypothesize that when the dipole of a symmetric solvent aligns with the electric field, the solvent molecule adopts a configuration that shields Li^+ from the surface, slowing down charge transfer due to steric hindrance (Fig. 5f). However, asymmetric solvents, with their 'tilted' dipoles, may be aligned under the electric field such that they shield Li^+ less from the anode surface. This could enhance redox kinetics, facilitating faster electron transfer to Li^+ and subsequent solvent release, accompanied by a stable SEI formation and homogeneous Li growth (Fig. 5g). Furthermore, we believe this phenomenon improves redox kinetics most when the solvent–Li^+ system can rotate quickly. For example, when the DEE–Li^+ system is aligned with the electric field,

https://doi.org/10.1038/s41560-025-01716-w

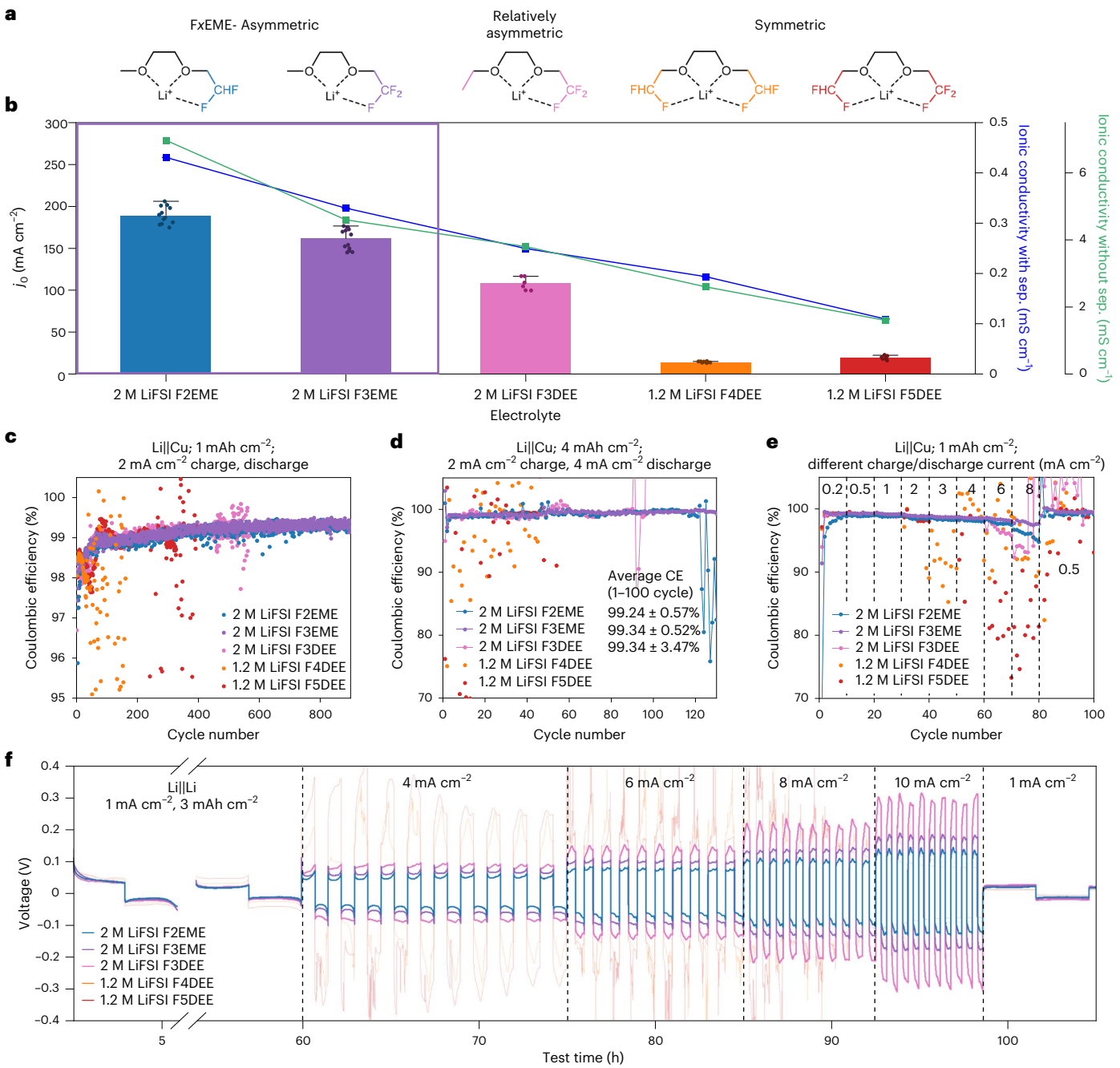

Fig. 4 | Comparison of electrolyte properties and high-rate Li^0 plating/stripping reversibility between F*x*EME and F*x*DEE. a, Structure of Li$^+$-coordinated F*x*EME and F*x*DEE. **b**, Exchange current density measurements (bar graph, sample size (n) = 6 for F*x*DEE and 12 for F*x*EME; each measurement performed with polished UME and separate transient voltammetry; data are presented as mean values ± SD) and ionic conductivity measurements (with (blue) and without (green) Celgard 2325 separator (sep.), n = 4; each measurement from different EIS curves; data are presented as mean values ± SD) of F*x*EME and F*x*DEE electrolytes. Asymmetric F2EME and F3EME (purple box) shows higher j_0 compared to F*x*DEE. **c**–**e**, High-rate Li || Cu cycling performance with three different conditions of 2 mA cm^{-2} charge/discharge and 1 mAh cm^{-2} areal capacity (**c**), 2 mA cm^{-2} charge / 4 mA cm^{-2} discharge and 4 mAh cm^{-2} areal capacity (**d**), different charge/discharge current density (0.2–8 mA cm^{-2}) with fixed areal capacity (1 mAh cm^{-2}) (**e**). **f**, Li || Li symmetric cells cycling with different current densities (1–10 mA cm^{-2}) and same areal capacity (3 mAh cm^{-2}). The voltage profiles exhibit similar trends in the x-axis break (5–55 h) under 1 mA cm^{-2} current density and 3 mAh cm^{-2} areal capacity.

the solvent may not shield Li$^+$ from the surface, which should increase redox kinetics. However, our data show that its j_0 is worse than both EME and MPE. This could be due to the relatively small dipole of the DEE–Li$^+$ system, leading to slow rotation, especially with steric hindrance from neighbouring molecules (Supplementary Fig. 44). The trend of higher j_0 for asymmetric solvents is seen for both fluorinated and non-fluorinated ethers. It is also seen that in general j_0 is higher for the non-fluorinated solvent compared to its fluorinated counterpart despite similar dipole angles. This is consistent with our hypothesis that solvent de-shielding is an important factor impacting charge transfer as the heavier fluorinated ether solvents are expected to move away more slowly. We also hypothesize that the asymmetric design may be applicable to other solvent classes. However, systematic investigations are still needed.

https://doi.org/10.1038/s41560-025-01716-w

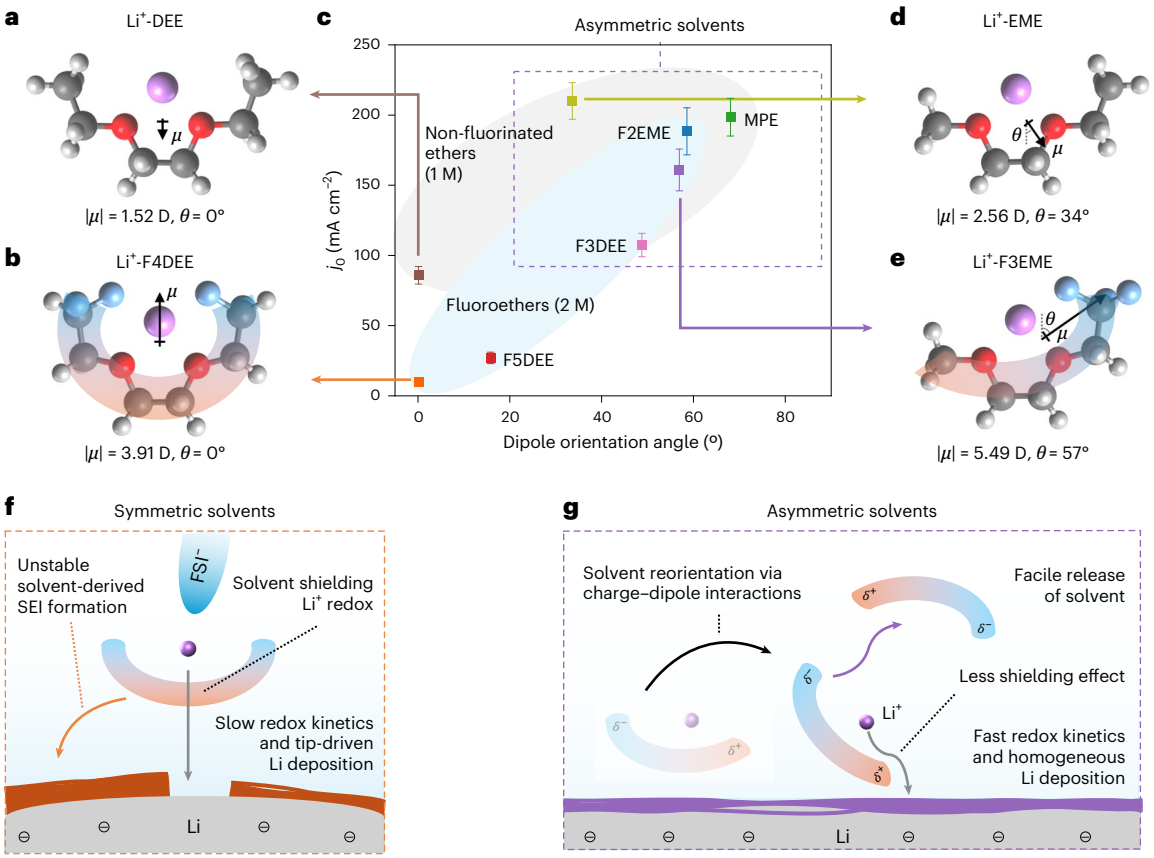

Fig. 5 | Proposed mechanism of asymmetric ether solvents showing fast redox kinetic. a,**b**,**d**,**e**, DFT calculations of ion-induced dipole moment (μ) of Li^+-coordinated ether solvents, including DEE (**a**), F4DEE (**b**), EME (**d**) and F3EME (**e**). The dipole moment of asymmetric solvents has more directionality towards ethyl or propyl tail compared to symmetric solvents. Directionality of μ can be indicated by the angle (θ) shown in the figures. **c**, Positive correlation between dipole orientation angle and j_0 within each class of solvent. The solvents investigated in this study are each represented by distinct colours, as shown in previous figures. j_0 values in this plot were from 1 M of non-fluorinated ethers (black shaded region) and 2 M of fluoroethers (blue shaded region) (sample size = 6 for F*x*DEE, EME, DEE and 9 for DME, MPE and 12 for F*x*EME; each measurement performed with polished UME and separate transient voltammetry; data are presented as mean values ± SD). **f**, Schematics of symmetric solvent showing slow redox kinetic and unstable solvent-derived SEI formation due to the solvent shielding effect. **g**, Schematics of asymmetric solvents providing fast redox kinetics and favourable SEI formation due to the dipole (δ)-induced solvent reorientation and less solvent shielding effect.

High-rate performance of Li-metal and anode-free full cells

We proceeded to evaluate the developed electrolytes for high-rate performance of Li-metal and anode-free full cells with three typical cathode chemistries (Supplementary Table. 4). We initiated our study by constructing Li-metal full cells with thin Li foil (20 µm) and an industrial high-loading LFP cathode (3 mAh cm^{-2}), a cost-effective material[56]. The use of 20 µm Li rather than the typical 50 µm Li allows for a more stringent evaluation of electrolyte properties, as the lower charge cut-off voltage of LFP compared to NMC811 reduces the emphasis on electrolyte oxidative stability. These cells were cycled at a high rate of 0.5 C charge and 1 C discharge to assess their initial capacity retention over cycles. Cycle life with 80% capacity retention followed the trend of: F3EME > F2EME > F3DEE > F4DEE ~ F5DEE (Fig. 6a), which is well aligned with the Li || Cu CE stability. Energy efficiency and voltage polarization are shown in Supplementary Figs. 46 and 47. As expected, those with higher j_0 and ionic conductivity gave more stable voltage polarization and higher energy efficiency.

High-voltage NMC811 cathodes were tested for higher energy density applications. Full cells were constructed by pairing 50-µm Li foil with 4.9 mAh cm^{-2} NMC811 cathode. We applied rate-step cycling from C/10 charge, C/3 discharge to 4 C charge, 4 C discharge (Fig. 6b and Supplementary Figs. 48). This testing aimed to determine the limits of each electrolyte under varied rate conditions. F4DEE and F5DEE started to show decreased capacity at C/2 charge and 1 C discharge, whereas F3DEE began at 1 C charge and 2 C discharge rate. In contrast, F3EME demonstrated resilience under high-rate conditions, delivering a relatively higher capacity of ~3 mAh cm^{-2} even at the demanding 4 C charge/discharge. For long-term cycling evaluations, we focused on the 0.5 C charge and 1 C discharge rates, considering the sustained performance for F3DEE and F3EME. Cycle life and energy efficiency were in the order of F3EME > F3DEE > F5DEE > F4DEE, which is again well aligned with j_0 and Li || Cu cycling results (Fig. 6c and Supplementary Figs. 49 and 51). Furthermore, LiDFP-assisted F3EME electrolytes showed cycling over 220 cycles, which stands among the best-performing electrolytes[57].

Further investigation extended to anode-free pouch cells utilizing different cathode chemistries, including microparticle–LFP, NMC532 and Ni95. These cells were cycled at high rates to determine the robustness of the developed electrolytes under stringent conditions (Fig. 6d–f). Cu || LFP and Cu || NMC pouch cells, cycled at 0.5 C charge and 2 C discharge for Cu || LFP and 0.5 C charge and 1 C discharge for Cu || NMC, again exhibited cycle life trends consistent with those observed in Li-metal full cells. The accompanying voltage profiles, voltage polarization and energy efficiency data further corroborated the superior performance of F3EME over F3DEE, F5DEE and F4DEE in these applications (Supplementary Figs. 50, 52and 53). LiDFP

https://doi.org/10.1038/s41560-025-01716-w

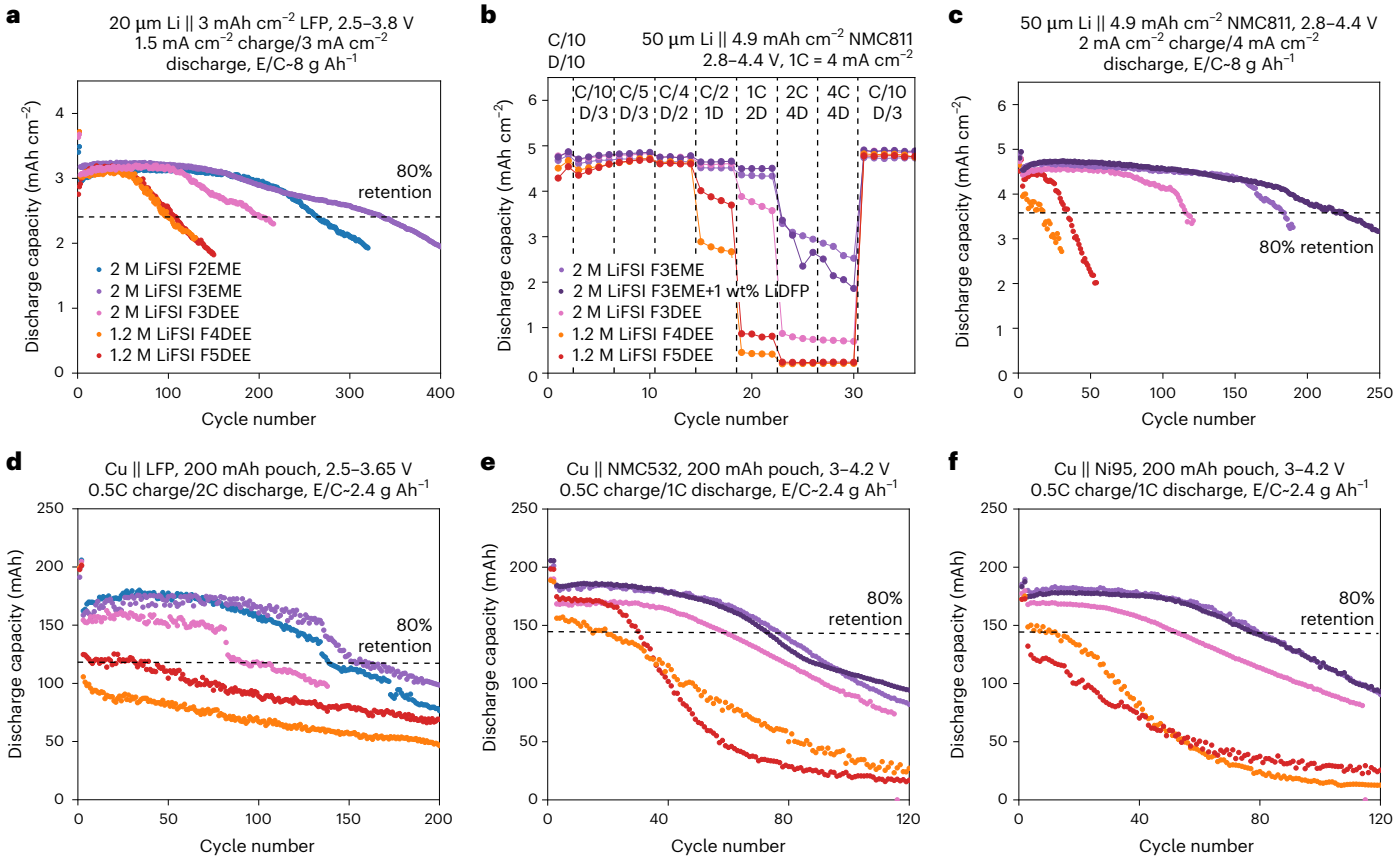

Fig. 6 | High-rate LMBs full-cell cycling with F*x*EME and F*x*DEE electrolytes. **a**, Long cycling performance of thin Li || high-loading LFP coin cells. Conditions: 20-µm thick Li, 3 mAh cm^{-2} LFP, 2.5–3.8 V, 0.5 C charge/1 C discharge and E/C = 8 g Ah^{-1}. **b**, Rate-step performance testing of Li || NMC811 coin cells. Conditions: 50-µm thick Li, 4.9 mAh cm^{-2} NMC811, 2.8–4.4 V, charge/discharge current densities from 0.1 C to 4 C (1 C = 4 mA cm^{-2}) and E/C = 8 g Ah^{-1}. **c**, Long cycling performance of Li || NMC811. Conditions: 50-µm thick Li, 4.9 mAh cm^{-2} NMC811, 2.8–4.4 V, 0.5 C charge/1 C discharge and E/C = 8 g Ah^{-1}. **d**–**f**, Long cycling performance of anode-free pouch cells (200 mAh) with different cathode chemistries, including Cu || microparticle–LFP anode-free industrial pouch cells (**d**, conditions: 2.5–3.65 V, 0.5 C charge / 2 C discharge and E/C ~ 2.4 g Ah^{-1}), Cu || NMC532 (**e**) or Ni95 (**f**) (conditions: 3–4.2 V, 0.5 C charge / 1 C discharge E/C ~ 2.4 g Ah^{-1}). Repeated cells are shown in Supplementary Fig. 45.

additive showed no substantial enhancement in cycle life for F3EME electrolyte, particularly given the lower voltage cut-off of 4.2 V and the anode-limiting cycle life. F3EME gave over 140 cycles for Cu || LFP and over 70 cycles for Cu || NMC before noticeable performance decline. These pouch cells exhibited no gassing issues underscoring their high safety compared to non-fluorinated electrolytes such as EME (Supplementary Fig. 54). Furthermore, fluoroethers demonstrated reduced flammability compared with non-fluorinated ethers and conventional electrolytes (Supplementary Fig. 55 and Supplementary Video 1).

Comparative evaluations were also conducted with LHCE (1LiFSI–1.2DME-3TTE), a benchmark electrolyte known for its performance in Li || NMC cells[58]. Neither Li || Cu nor Li || NMC configurations could sustain long cycles under high-rate cycling conditions with LHCE (Supplementary Figs. 56 and 57).

Application of eVTOL protocol

Electric vertical take-off and landing (eVTOL) aircraft have emerged as promising candidates for urban mobility, necessitating batteries with high energy density for extended range and robust power delivery for frequent take-off and landing manoeuvres[33,59,60]. Among the electrolytes studied, F3EME demonstrated potential for supporting high-rate LMBs, making it particularly suitable for eVTOL applications.

We first systematically evaluated the F*x*EME and F*x*DEE electrolytes across five critical performance metrics for high-rate operation: ionic conductivity, kinetics, interfacial stability, oxidative stability and overpotential (Fig. 7a and Supplementary Table. 6). Compared to F*x*DEE, which exhibited inferior kinetics and lower ionic conductivity, the F3EME showed more balanced performance characteristics, as corroborated by full-cell cycling and subsequent testing with eVTOL battery protocol demonstrating reduced power fade.

The eVTOL battery protocol was designed based on recent studies of lithium battery applications in eVTOL aircraft, involving demanding discharge conditions (Fig. 7b)[29]. On the basis of this protocol, state-of-charge (SOC) utilization ranged from approximately 50% to 90% of total capacity, with the discharge voltage profiles of Cu || Ni95 pouch cells shown in Fig. 7c. It is important to monitor end-of-discharge voltage, which is an indication of terminal achievable power to assess power fade. An end voltage below 2.8 V indicates the cell can no longer deliver sufficient power to complete the landing, thereby reaching its end of life. Initially, anode-free Cu || Ni95 pouch cells were cycled using the eVTOL protocol due to their ability to achieve high energy density. Charging at 0.5 C to 4.2 V followed by eVTOL discharge cycles revealed distinct performance differences among the electrolytes (Fig. 7d). F4DEE and F5DEE exhibited limited cycle life, characterized by substantial end-of-discharge voltage decay and overpotential growth. F3DEE exhibited acceptable cycling performance but experienced notable power decay after approximately 350 cycles. Remarkably, F3EME enabled anode-free pouch cells to cycle over 600 cycles with energy efficiency exceeding 90%, demonstrating minimal power decay and polarization growth (Fig. 7d,e). Instances of power decay were

https://doi.org/10.1038/s41560-025-01716-w

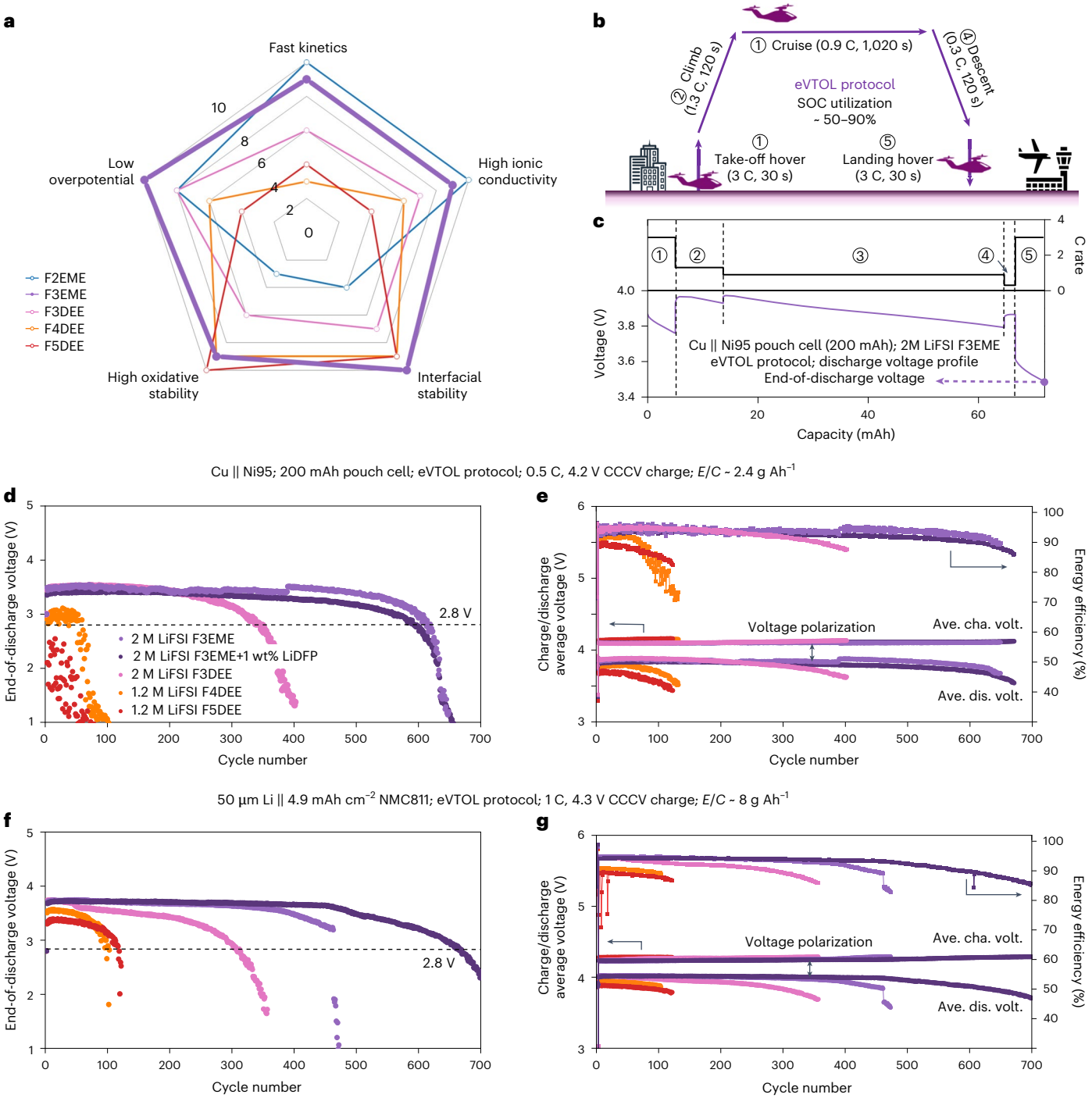

Fig. 7 | Superior high-rate LMBs performance of F3EME electrolyte and its practicality tests using eVTOL protocol. a, Radar plot with five requirements for high-rate LMBs (fast kinetics, high ionic conductivity, SEI compactness, high oxidative stability, low overpotential) to evaluate F*x*EME and F*x*DEE electrolytes. Ratings of 1 to 10 ratings are given to each electrolyte (10 stands for ideal properties) and rationale for ratings are shown in Supplementary Table. 6. **b**,**c**, Specified discharge protocol mimicking eVTOL scenario[29] (**b**) and the voltage profile of Cu || Ni95 following this protocol (**c**). **d**,**e**, Cu || Ni95 anode-free pouch cells (200 mAh) cycled with eVTOL discharge protocol and 0.5 C, 4.2 V constant-current-constant-voltage (CCCV) charge. End-of-discharge voltage is shown as an indicative of cycle life (**d**) and average charge voltage (Ave. cha. volt.), average discharge voltage (Ave. dis. volt.) and energy efficiency over cycles are shown (**e**). **f**,**g**, 50-μm Li || 4.9 mAh cm^{-2} NMC811 was cycled with eVTOL discharge protocol and 1 C, 4.3 V-CCCV charge. End-of-discharge voltage was shown as an indicative of cycle life (**f**) and average charge, discharge voltage and energy efficiency over cycles are shown (**g**). Repeated cells are shown in Supplementary Figs. 58.

potentially linked to SEI accumulation and electrolyte consumption, notwithstanding intact Ni95 cathode particles (Supplementary Fig. 59).

Further evaluation involved LMB coin cells (50-μm Li | |4.9 mAh cm^{-2} NMC811) subjected to the eVTOL protocol under stringent conditions of 1 C charging and a 4.3 V voltage cut-off (Fig. 7f). The trend in power decay mirrored that observed in anode-free pouch cells, with F3EME + LiDFP exhibiting the longest cycle life up to 550 cycles, characterized by minimal voltage polarization growth and stable energy efficiency. Energy efficiency followed the trend of ionic conductivity: F3EME > F3DEE > F4DEE > F5DEE (Fig. 7g), whereas end-of-discharge voltage decay aligned with exchange current density: F3EME > F3DEE > F5DEE > F4DEE (Fig. 7f and Supplementary

Figs. 60 and 61). The asymmetric structure of F3EME gave both enhanced exchange current density and ionic conductivity, rendering it well-suited for high-rate LMBs in eVTOL applications (Supplementary Table 5).

Additionally, SEM analysis of Li plating morphology (Supplementary Fig. 64) after eVTOL protocol revealed that F3EME facilitated compact lithium deposition below the rSEI layer with a grain size of approximately 20 µm. In contrast, F*x*DEE electrolytes exhibited SEI fractures and lithium growth predominantly on top of the SEI layer, probably due to plating through pin holes in the non-uniform rSEI layer[61].

Conclusion

In this work, we engineered asymmetric fluorinated ether electrolytes tailored for high-rate LMBs. Our investigation revealed that the solvent asymmetry resulted in faster Li redox kinetics. We proposed that high directionality of ion (Li^+)-induced dipole moment in asymmetric solvents reorients the solvation structure near the negatively charged Li surface, leading to less solvent shielding and higher j_0. Among the developed electrolytes, F3EME exhibited superior characteristics, including high exchange current density, enhanced ionic conductivity and robust oxidative stability. These attributes collectively contributed to prolonged cycle life in both LMBs (220 cycles, 2 mA cm^{-2} charge / 4 mA cm^{-2} discharge for 4.9 mAh cm^{-2} NMC811) and anode-free pouch cells (140 cycles for Cu || LFP, 0.5 C charge / 2 C discharge), even under conditions of reduced electrolyte volume and realistic operational testing. Furthermore, our application of an eVTOL protocol demonstrated the practicality of F3EME, showcasing its capability to sustain anode-free pouch cells through more than 600 cycles. The asymmetric F3EME molecule opens new possibilities for designing electrolytes with both high ionic conductivity and fast-charge transfer kinetics. This study provides understanding of the performance and durability of next-generation Li-metal battery technologies, with implications extending to various high-power applications including aerospace and beyond.

Methods

General materials

2-ethoxy ethanol was purchased from Sigma-Aldrich, ethylene glycol monopropylether was purchased from Merck KGaA. 2,2,2-trifluoro ethyl p-toluenesulfornate and 2,2-difluoroethanol were purchased from Synquest Lab. 2-fluoroethanol was purchased from Matrix Scientific. Ethylene carbonate, p-toluenesulfonyl chloride, sodium hydride (60% in mineral oil), methyl iodide, tetraglyme, triethyl amine and other general reagents were purchased from Sigma-Aldrich, Fisher Scientific or TCI. All chemicals for reactions were used as prepared. LiFSI was obtained from Solvionic. DME (99.5%, anhydrous) and DEE (99%, anhydrous) were purchased from Sigma-Aldrich and used as received.

The commercial Li battery separator Celgard 2325 (25 µm thick, consisting of polypropylene/polyethylene/polypropylene layers) was procured from Celgard and utilized in all coin cells. Thick Li foil (500-µm thick) and Cu current collector (25-µm thick) were obtained from Alfa Aesar. Thin Li foils (50-µm and 20-µm thick) were sourced from China Energy Lithium. Commercial cathode sheets including LFP (~ 3 mAh cm^{-2}) and NMC811 (~ 4.9 mAh cm^{-2}) were purchased from Targray. Industrial-grade dry Cu || LFP, Cu || NMC532 and Cu || Ni95 pouch cells (200-mAh capacity) were obtained from Li-Fun Technology. Other necessary battery components such as 2032-type coin cell cases, cone springs, spacers and Al-clad cases were all acquired from MTI.

Synthesis and electrolyte preparation

For EME, to a 1-l round flask was added 27.9 g of 2-ethoxy ethanol, 57.2 g of MeI, 61.8 g of NaOH and 400 ml tetrahydrofuran (THF) (Supplementary Figs. 65 and 66). The suspension was stirred at room temperature for 2 h, the flask was heated up to 60 °C to reflux for 2 days. The suspension was filtered and the remaining THF in the resulting solution was removed under rotary evaporator. The product underwent vacuum distillation (vapour temperature ~30–35 °C at ~90 mbar) four times to obtain colourless liquid as the product. Yield: roughly 55%.

For MPE, the same procedure as for EME synthesis was adopted, except that 27.9 g of 2-ethoxy ethanol was replaced by 32.2 g of ethylene glycol monopropylether (Supplementary Figs. 65, 67). The product underwent vacuum distillation (vapour temperature ~40-45 °C at ~90 mbar) four times to remove remaining THF. Yield: roughly 65%.

For F1EME, 2-fluoroethyl tosylate was synthesized first following the method described in ref. 62. 2-fluoroethanol (19.2 g, 0.300 mol), p-toluenesulfonyl chloride (60.05 g, 0.315 mol), triethyl amine (45.9 ml, 0.33 mol) and 200 ml of DCM were added to a 500 ml round-bottom flask in an ice bath. The mixture was stirred at room temperature for 24 h, washed sequentially with 300 ml of aqueous $NaHCO_3$ solution, DI water (2 × 300 ml) and brine (300 ml). The organic phase was dried over anhydrous Na_2SO_4 and concentrated by rotary evaporation to yield a pale orange liquid. F1EME was obtained via the reaction of 2-methoxyethanol (7.05 g, 0.927 mol) with the synthesized 2-fluoroethyl tosylate (21.12 g, 0.973 mol) in 200 ml of dry THF (Supplementary Figs. 68 and 69). The mixture, cooled in an ice bath, was treated with NaH (4.67 g, 60%, 0.116 mol) and stirred for 2 h before refluxing overnight at 60 °C. After cooling, the mixture was filtered and the filtrate was purified by vacuum distillation (vapour temperature ~0–5 °C at ~90 mbar) for four times to obtain a pure and colourless F1EME. Yield: roughly 40%.

For F2EME, 2-(2,2-difluoroethoxy) ethanol was synthesized first (same method described in ref. 20). The suspension of 2,2-difluoroethanol (75 g, 0.914 mol), ethylene carbonate (70 g, 0.795 mol), NaOH (4 g) and tetraglyme (100 ml) were heated to 140 °C for 72 h. The resulting black colour suspension was distilled under vacuum three times to yield a colourless liquid. F2EME was synthesized via methoxylation of the product (Supplementary Figs. 68 and 70). A mixture of 2-(2,2-difluoroethoxy) ethanol (30 g, 0.238 mol), methyl iodide (67.6 g, 0.476 mol), NaOH (63.4 g, 1.189 mol) and 400 ml of THF was stirred at room temperature for 2 h, then refluxed at 60 °C for 2 days. The suspension was filtered, and the THF was removed by rotary evaporation. Four times of vacuum distillation (vapour temperature ~70–75 °C at ~90 mbar) yielded pure, colourless F2EME. Yield: roughly 80%.

For F3EME, to a 500 ml round flask was added 22.8 g (0.300 mol) of 2-methoxyethanol was dissolved with 200 ml dry THF and the solution was cooled with an ice bath (Supplementary Figs. 68 and 71). NaH (14.4 g, 60%, 0.360 mmol) was added and stirred for 2 h, after which 2,2,2-trifluoro ethyl p-toluenesulfornate (80.0 g, 0.315 mol) was added. The resulting mixture was further stirred for 2 h and then refluxed overnight at 60 °C. The suspension was filtered and rinsed with THF after cooling at room temperature. Then, filtered solution underwent vacuum distillation (vapour temperature ~45–50 °C at 90 mbar) for four times to obtain a colourless liquid as the product. Yield: roughly 55%.

For F*x*DEE ($x = 3, 4, 5$), solvents were synthesized with same method described in ref. 20.

All the purchased or synthesized solvents were treated with Li for further purification. Electrolytes were prepared by dissolving LiFSI (374.2 mg) in 1 ml of F*x*EME or F3DEE to obtain the 2 M LiFSI electrolytes and LiFSI (187.1 mg) in 1 ml of DME, EME, MPE, DEE to obtain the 1 M LiFSI electrolytes. 224.4 mg of LiFSI was dissolved in 1 ml of F4DEE and F5DEE to obtain 1.2 M LiFSI electrolytes. All the solvents and electrolytes were prepared and stored in an argon-filled glovebox ($O_2 < 1$ ppm, water <0.1 ppm) at room temperature.

Theoretical calculations

Molecular structures were optimized using density functional theory (DFT) at the B3LYP/aug-cc-pVDZ level with Gaussian16[63]. These structures were used to determine the dipole orientations shown in this work. GaussView 6[64] and Avogadro 1.2[65] were used to visualize these systems.

The choice of functional and basis set was influenced by previous work on calculating dipole moments using DFT, which recommended 'using a hybrid functional with an augmented double-ζ-quality basis from the Jensen or Dunning families' to achieve a reasonable balance between accuracy and computational efficiency[66,67].

Classical, fixed-charge molecular dynamic (MD) simulations were conducted using LAMMPS. Each system was initially constructed in random, amorphous configurations of ~500 total molecules whose molecular ratios match the experimental molar component ratios and periodic boundary conditions in all directions. All system components were described using the General Amber forcefield with partial charges generated with the AM1-BCC method in ANTECHAMBER[68]. Non-bonded interactions not defined by the forcefields were generated using Lorentz–Berthelot mixing rules. In all cases the charges of the ionic species were scaled to 0.75, with a 10 Å cut-off for Van der Waals and real space Coulomb interactions. Long-range Coulomb interactions were computed with a particle–particle–particle–mesh solver, with an error tolerance of 10^{-3}.

Before any dynamics were simulated, an initial energy minimization at 0 K was performed with energy and force tolerances of 10^{-4}. The system was then heated to 298 K at constant volume over 0.01 ns using a Langevin thermostat, with a damping parameter of 100 ps. To eliminate any meta-stable solvation states, five cycles of quench-annealing dynamics were then applied, where the system temperature was cycled between 298 K and 894 K with a ramp period 0.025 ns followed by 0.1 ns of dynamics at either temperature extreme, also at constant volume. Next, a constant temperature, constant pressure ensemble was applied using the Andersen barostat for 1.5 ns with a pressure relaxation constant of 1 ps to allow for equilibration of the system density. Finally, 10 ns of constant volume, constant temperature production dynamics at 298 K was performed, again using a Langevin thermostat with a damping parameter of 100 ps. Radial distribution functions were calculated during this period. Snapshots of Li^+ solvation shells were captured using the Visual Molecular Dynamics (VMD) software[69] using trajectories generated from the production dynamics. The SolvationAnalysis package was used to analyse ion speciation and solvation shells from the production run[70].

Materials characterization

Various analytical techniques were employed in this study: ^{1}H-, ^{13}C- and ^{19}F-NMR (nuclear magnetic resonance) spectra, along with heteronuclear single quantum coherence spectra, were recorded using a Varian 400 MHz, 100 MHz, 376 MHz NMR spectrometer, respectively. Viscosity measurements were conducted at 25 °C using a 'Rheometer-on-a-chip' (model m-VROC-II). Raman spectra were acquired using a Horiba XploRA+ confocal Raman system equipped with a diamond attenuated total reflectance attachment and a 532 nm source. SEM and FIB-SEM images were obtained using Thermo Fisher Scientific Apreo S LoVac and FEI Helios NanoLab 600i DualBeam instruments, respectively. For XPS measurements, residual SEI samples (20 cycled Li || Cu configurations with varying current densities, where lithium was fully stripped from copper) were washed with DME for 10 s to remove residual electrolytes. Subsequently, the samples were transferred and sealed in an XPS holder within an argon-filled glovebox. XPS profiles were then measured using PHI VersaProbe 3 or PHI VersaProbe 4 equipment.

H_2O titration techniques were done for rSEI (20 cycled Li || Cu with 0.5 mA cm^{-2} current density and 1 mAh cm^{-2} areal capacity, Li fully stripped from Cu) to measure the amount of inactive Li. One ml H_2O is added to one sheet of rSEI on Cu in 10 ml sealed vial. After reacting for 3 min, generated H_2 gas amount was quantified with gas chromatography (SRI 8610 C).

Solvation free energy and entropy were measured according to our recent work[36,71]. For solvation free energy measurements, four layers of Celgard 2325 were inserted in the two junctions between a T-shaped glass flange and an H cell, with each of the three chambers containing a different electrolyte (test, reference and salt bridge) and lithium electrodes placed at each side of the H cell. The open-circuit voltage (OCV) between the electrodes was measured using a Biologic system. For entropy measurements, a single layer of Celgard 2325 was positioned in the bridge of the H cell, with each half cell containing a lithium-metal electrode and a thermocouple located near the electrode surface. A Kapton heater wrapped around one half cell provided controlled power from a d.c. source, and the OCV was measured with the Biologic system.

DOSY NMR (diffusion ordered spectroscopy nuclear magnetic resonance) was performed on Varian 400 MHz spectrometer at 25 °C. ^{7}Li-, ^{19}F- and ^{1}H-pulsed field gradient measurements were performed to determine the self-diffusion coefficients of Li^+, FSI^- and solvent using dbppste_cc, pgste and pgste pulse sequences, respectively. The array of gradient strength was set to 2.908 to 12.504 G cm^{-1} with 12 linear steps. Appropriate diffusion delay (Δ) and gradient pulse duration (δ) were selected to ensure sufficient signal decay. Self-diffusion coefficients were calculated by fitting peak integrals to the Stejskal–Tanner equation.

Cryogenic transmission electron microscopy

During the construction of each cell, a 400-mesh Cu transmission electron microscope (TEM) grid was positioned in the coin cell stack on top of the Cu current collector. After lithium plating, the cell was then deconstructed inside an Ar glovebox to prevent exposure to air and moisture. The grid was washed with the 1,2-dimethoxyethane (DME) to remove excess salts from the grid and was left to dry in the glovebox (~120 s). Next, the grid was quickly (~2 s) transferred out of the Ar glovebox in a plastic Falcon Tube and immersed in a container filled with liquid nitrogen (LN2). Pliers were used to break open the plastic tube under LN2, and the Cu grid was transferred to a LN2 dewar. Still under LN2, the Cu grid was taken out of the dewar and placed into a cryo-holder (Gatan 626) with the use of a cryo-transfer station to ensure an air-free transfer. Finally, the cryo-holder was quickly removed from the transfer station and inserted into the TEM column (~1 s); once inside the column the temperature was maintained at −172 °C during the imaging session.

All cryo-TEM images were captured on the FEI Titan 80-300 environmental (scanning) TEM, equipped with an aberration corrector in the objective lens. Moreover, all images were captured at an accelerating voltage of 300 kV and full alignments were performed before each imaging session.

Electrochemical measurements

The methods employed in this study utilized commercially available battery components and various electrochemical set-ups including ultra-micro-electrodes (UME), Swagelok-cells, 2032-type coin cells and pouch cells. Coin cells were assembled in an Ar-filled glovebox using Celgard 2325 as the separator. For the different cell configurations, we used Al-clad coin cell cases for Li || NMC811, Li || LFP and Li || Al cells; Pt-coated cases for Li || Pt cells and stainless-steel cases for other cell types.

Electrochemical tests such as transient voltammetry, electrochemical impedance spectroscopy (EIS), linear sweep voltammetry (LSV) and lithium-ion transference number measurements were conducted using a Biologic system. Cycling tests for coin cells and pouch cells were performed using a LAND cycler or Arbin instrument.

For transient cyclic voltammetry, a previously established method was followed using home-built tungsten disc UME[35]. UMEs were built by sealing a 12.5-µm wire into a polypropylene. In the experimental set-up, the UME served as the working electrode, whereas a Li-metal chip attached to the coin cell case served as the counter/reference electrode. The measurement of iR_u drop (R_u, uncompensated resistance) was conducted using EIS at a frequency of 100 kHz, compensating with positive feedback. Voltage was linearly swept from the open-circuit

voltage (OCV) to −1 or −2 V at scan rates of 150, 200 V s^{-1}, followed by a return to OCV. EIS measurements were conducted over a frequency range from 1 MHz to 100 mHz, and GEIS (galvanostatic electrochemical impedance spectroscopy) measurements involved sequential current density increases during lithium plating on Cu, applying a 400-µA current amplitude wave over a frequency range from 200 kHz to 0.1 Hz. LSV tests spanned from OCV to 6.5 V in Li || Al or Li || Pt cells. Li^+ transference number was determined using the Bruce–Vincent method[72] with a 10 mV constant-voltage bias in Li || Li cells.

The Aurbach Coulombic Efficiency (CE) test[37,38] followed a standard protocol: first, an initial formation cycle was conducted by depositing 5 mAh cm^{-2} of lithium on copper (Cu) under a current density of 0.5 mA cm^{-2}, followed by stripping to 1 V. Second, a lithium reservoir of 5 mAh cm^{-2} was deposited on Cu at the same current density. Third, lithium was repeatedly deposited and stripped in cycles of 1 mAh cm^{-2} under 0.5 mA cm^{-2} for ten cycles. Finally, all lithium was stripped to 1 V to complete the test procedure. In the Li || Cu half cell CE tests, the procedure began with ten pre-cycles between 0 and 1 V to clean the Cu electrode surface. Subsequently, cycling involved depositing either 1 (or 4) mAh cm^{-2} of Li onto the Cu electrode at various current densities ranging from 0.2 to 8 mA cm^{-2}, followed by stripping to 1 V. The CE was determined by dividing the total stripping capacity by the total deposition capacity. Li || Li symmetric cells were cycled using different current density (1–10 mA cm^{-2}) and 1 (or 3) areal capacity.

The cycling protocols for different battery configurations were as follows: Li | |NMC or LFP coin cells underwent initial activation with two cycles at 0.1 C charge/discharge rates before cycling at varying rates. Subsequent cycles utilized a constant-current-constant-voltage (CCCV) method, charging the cells to their upper voltage limits and holding until current dropped below 0.1 C. Voltage ranges were 2.8–4.4 V for NMC cathodes and 2.5–3.8 V for LFP cathodes, with an electrolyte to cathode ratio (E/C) of approximately 8 g Ah^{-1}. Cu || LFP anode-free pouch cells were cycled after two activation cycles (0.1 C charge / 0.5 C discharge for the first and 0.2 C charge / 0.5 C discharge thereafter) at varying rates, with a voltage range of 2.5–3.65 V. Cu || NMC532 or Ni95 anode-free pouch cells underwent two activation cycles at 0.1 C charge / 0.3 C discharge before cycling at 0.5 C charge / 1 C discharge rates. CCCV protocol was used at the end of charging, with a voltage range of 3–4.2 V. All pouch cells were clamped at approximately 1,000 kPa with acrylate plates and cycled under ambient conditions. E/C ratio was approximately 2.4 g Ah^{-1}.

Both Cu || Ni95 anode-free pouch cells and Li || NMC811 coin cells were subjected to the eVTOL discharge protocol following two initial activation cycles as previously described. Full-cell cycling utilized a reported eVTOL protocol[29] (as per ref. 28): beginning with a discharge sequence of 3 C for 30 s, followed by 1.3 C for 120 s, 0.9 C for 1,020 s, 0.3 C for another 120 s and concluding with 3 C discharge for 30 s (1 C = 200 mA for Cu || Ni95 and 4 mA for Li || NMC811). During charging, various rates (ranging from 0.5 to 3 C) were applied using a constant-current-constant-voltage (CCCV) protocol set to 4.2 V for Cu || Ni95 cells and 4.3 V for Li || NMC811 cells.

Data availability

All relevant data are included in the paper and its Supplementary Information. Source data are provided with this paper.

Code availability

The code and data used to determine dipole orientations is available at https://github.com/Adi1008/asymmetric-solvents.

References

1. Albertus, P., Babinec, S., Litzelman, S. & Newman, A. Status and challenges in enabling the lithium metal electrode for high-energy and low-cost rechargeable batteries. *Nat. Energy* **3**, 16–21 (2018).
2. Liu, J. et al. Pathways for practical high-energy long-cycling lithium metal batteries. *Nat. Energy* **4**, 180–186 (2019).
3. Cheng, X. B. et al. A review of solid electrolyte interphases on lithium metal anode. *Adv. Sci.* **3**, 1500213 (2016).
4. Sayavong, P. et al. Dissolution of the solid electrolyte interphase and its effects on lithium metal anode cyclability. *J. Am. Chem. Soc.* **145**, 12342–12350 (2023).
5. Boyle, D. T. et al. Resolving current-dependent regimes of electroplating mechanisms for fast charging lithium metal anodes. *Nano Lett.* **22**, 8224–8232 (2022).
6. Lin, D., Liu, Y. & Cui, Y. Reviving the lithium metal anode for high-energy batteries. *Nat. Nanotech.* **12**, 194–206 (2017).
7. Hobold, G. M. et al. Moving beyond 99.9% Coulombic efficiency for lithium anodes in liquid electrolytes. *Nat. Energy* **6**, 951–960 (2021).
8. Xiao, J. et al. Understanding and applying coulombic efficiency in lithium metal batteries. *Nat. Energy* **5**, 561–568 (2020).
9. Yamada, Y., Wang, J., Ko, S., Watanabe, E. & Yamada, A. Advances and issues in developing salt-concentrated battery electrolytes. *Nat. Energy* **4**, 269–280 (2019).
10. Qian, J. et al. High rate and stable cycling of lithium metal anode. *Nat. Commun.* **6**, 6362 (2015).
11. Cao, X., Jia, H., Xu, W. & Zhang, J.-G. Localized high-concentration electrolytes for lithium batteries. *J. Electrochem. Soc.* **168**, 010522 (2021).
12. Li, G.-X. et al. Enhancing lithium-metal battery longevity through minimized coordinating diluent. *Nat. Energy* **9**, 817–827 (2024).
13. Zhang, H. et al. Electrolyte additives for lithium metal anodes and rechargeable lithium metal batteries: progress and perspectives. *Angew. Chem. Int. Ed.* **57**, 15002–15027 (2018).
14. Yang, G. et al. Improving the cyclability performance of lithium-ion batteries by introducing lithium difluorophosphate ($LiPO_2F_2$) additive. *RSC Adv.* **7**, 26052–26059 (2017).
15. Kim, S. C. et al. High-entropy electrolytes for practical lithium metal batteries. *Nat. Energy* **8**, 814–826 (2023).
16. Wang, Q. et al. High entropy liquid electrolytes for lithium batteries. *Nat. Commun.* **14**, 440 (2023).
17. Yu, Z. et al. Molecular design for electrolyte solvents enabling energy-dense and long-cycling lithium metal batteries. *Nat. Energy* **5**, 526–533 (2020).
18. Wang, Y. et al. Fluorination in advanced battery design. *Nat. Rev. Mater.* **9**, 119–133 (2024).
19. Chen, Y. et al. Steric effect tuned ion solvation enabling stable cycling of high-voltage lithium metal battery. *J. Am. Chem. Soc.* **143**, 18703–18713 (2021).
20. Yu, Z. et al. Rational solvent molecule tuning for high-performance lithium metal battery electrolytes. *Nat. Energy* **7**, 94–106 (2022).
21. Holoubek, J. et al. Tailoring electrolyte solvation for Li metal batteries cycled at ultra-low temperature. *Nat. Energy* **6**, 303–313 (2021).
22. Zhang, G. et al. A monofluoride ether-based electrolyte solution for fast-charging and low-temperature non-aqueous lithium metal batteries. *Nat. Commun.* **14**, 1081 (2023).
23. Ko, S. et al. Electrode potential influences the reversibility of lithium-metal anodes. *Nat. Energy* **7**, 1217–1224 (2022).
24. Diederichsen, K. M., McShane, E. J. & McCloskey, B. D. Promising routes to a high Li^+ transference number electrolyte for lithium ion batteries. *ACS Energy Lett.* **2**, 2563–2575 (2017).
25. Logan, E. & Dahn, J. Electrolyte design for fast-charging Li-ion batteries. *Trends Chem.* **2**, 354–366 (2020).
26. Holoubek, J. et al. Toward a quantitative interfacial description of solvation for Li metal battery operation under extreme conditions. *Proc. Natl Acad. Sci. USA* **120**, e2310714120 (2023).

27. Sheng, L. et al. Suppressing electrolyte-lithium metal reactivity via Li^+-desolvation in uniform nano-porous separator. *Nat. Commun.* **13**, 172 (2022).
28. Liang, P. et al. Competitive coordination of ternary anions enabling fast Li-ion desolvation for low-temperature lithium metal batteries. *Adv. Funct. Mater.* **34**, 2309858 (2024).
29. Yang, X.-G., Liu, T., Ge, S., Rountree, E. & Wang, C.-Y. Challenges and key requirements of batteries for electric vertical takeoff and landing aircraft. *Joule* **5**, 1644–1659 (2021).
30. Jiao, S. et al. Stable cycling of high-voltage lithium metal batteries in ether electrolytes. *Nat. Energy* **3**, 739–746 (2018).
31. Li, A.-M. et al. Asymmetric electrolyte design for high-energy lithium-ion batteries with micro-sized alloying anodes. *Nat. Energy* **9**, 1551–1560 (2024).
32. Von Aspern, N., Röschenthaler, G. V., Winter, M. & Cekic-Laskovic, I. Fluorine and lithium: ideal partners for high-performance rechargeable battery electrolytes. *Angew. Chem. Int. Ed.* **58**, 15978–16000 (2019).
33. Hatherall, O., Barai, A., Niri, M. F., Wang, Z. & Marco, J. Novel battery power capability assessment for improved eVTOL aircraft landing. *Appl. Energy* **361**, 122848 (2024).
34. Boyle, D. T. et al. Transient voltammetry with ultramicroelectrodes reveals the electron transfer kinetics of lithium metal anodes. *ACS Energy Lett.* **5**, 701–709 (2020).
35. Boyle, D. T. et al. Correlating kinetics to cyclability reveals thermodynamic origin of lithium anode morphology in liquid electrolytes. *J. Am. Chem. Soc.* **144**, 20717–20725 (2022).
36. Wang, H. et al. Correlating Li-ion solvation structures and electrode potential temperature coefficients. *J. Am. Chem. Soc.* **143**, 2264–2271 (2021).
37. Aurbach, D., Gofer, Y. & Langzam, J. The correlation between surface chemistry, surface morphology, and cycling efficiency of lithium electrodes in a few polar aprotic systems. *J. Electrochem. Soc.* **136**, 3198 (1989).
38. Adams, B. D., Zheng, J., Ren, X., Xu, W. & Zhang, J. G. Accurate determination of Coulombic efficiency for lithium metal anodes and lithium metal batteries. *Adv. Energy Mater.* **8**, 1702097 (2018).
39. Park, S., Kim, S., Lee, J.-A., Ue, M. & Choi, N.-S. Liquid electrolyte chemistries for solid electrolyte interphase construction on silicon and lithium-metal anodes. *Chem. Sci.* **14**, 9996–10024 (2023).
40. Huang, A. et al. Low-temperature and fast-charging lithium metal batteries enabled by solvent–solvent interaction mediated electrolyte. *Nano Lett.* **24**, 7499–7507 (2024).
41. Xu, K. 'Charge-transfer' process at graphite/electrolyte interface and the solvation sheath structure of Li^+ in nonaqueous electrolytes. *J. Electrochem. Soc.* **154**, A162 (2007).
42. Xue, W. et al. Ultra-high-voltage Ni-rich layered cathodes in practical Li metal batteries enabled by a sulfonamide-based electrolyte. *Nat. Energy* **6**, 495–505 (2021).
43. Wu, L.-Q. et al. Unveiling the role of fluorination in hexacyclic coordinated ether electrolytes for high-voltage lithium metal Bbatteries. *J. Am. Chem. Soc.* **146**, 5964–5976 (2024).
44. Fang, C. et al. Quantifying inactive lithium in lithium metal batteries. *Nature* **572**, 511–515 (2019).
45. Deng, W. et al. Quantification of reversible and irreversible lithium in practical lithium-metal batteries. *Nat. Energy* **7**, 1031–1041 (2022).
46. Wang, H. et al. Efficient lithium metal cycling over a wide range of pressures from an anion-derived solid–electrolyte interphase framework. *ACS Energy Lett.* **6**, 816–825 (2021).
47. Huang, W., Wang, H., Boyle, D. T., Li, Y. & Cui, Y. Resolving nanoscopic and mesoscopic heterogeneity of fluorinated species in battery solid-electrolyte interphases by cryogenic electron microscopy. *ACS Energy Lett.* **5**, 1128–1135 (2020).
48. Guo, R. & Gallant, B. M. Li_2O solid electrolyte interphase: probing transport properties at the chemical potential of lithium. *Chem. Mater.* **32**, 5525–5533 (2020).
49. Wang, C. et al. Lithium difluorophosphate as a promising electrolyte lithium additive for high-voltage lithium-ion batteries. *ACS Appl. Energy Mater.* **1**, 2647–2656 (2018).
50. Niu, C. et al. Balancing interfacial reactions to achieve long cycle life in high-energy lithium metal batteries. *Nat. Energy* **6**, 723–732 (2021).
51. Zheng, J. et al. Regulating electrodeposition morphology of lithium: towards commercially relevant secondary Li metal batteries. *Chem. Soc. Rev.* **49**, 2701–2750 (2020).
52. Lin, L. et al. Regulating lithium nucleation at the electrolyte/electrode interface in lithium metal batteries. *Adv. Funct. Mater.* **34**, 2315201 (2024).
53. Eftekhari, A. Energy efficiency: a critically important but neglected factor in battery research. *Sustain. Energy Fuels* **1**, 2053–2060 (2017).
54. Bai, P., Li, J., Brushett, F. R. & Bazant, M. Z. Transition of lithium growth mechanisms in liquid electrolytes. *Energy Environ. Sci.* **9**, 3221–3229 (2016).
55. Sand, H. J. III. On the concentration at the electrodes in a solution, with special reference to the liberation of hydrogen by electrolysis of a mixture of copper sulphate and sulphuric acid. *London Edinburgh Philos. Mag. J. Sci.* **1**, 45–79 (1901).
56. Berg, H. & Zackrisson, M. Perspectives on environmental and cost assessment of lithium metal negative electrodes in electric vehicle traction batteries. *J. Power Sources* **415**, 83–90 (2019).
57. Li, Z. et al. Critical review of fluorinated electrolytes for high-performance lithium metal batteries. *Adv. Funct. Mater.* **33**, 2300502 (2023).
58. Ren, X. et al. Enabling high-voltage lithium-metal batteries under practical conditions. *Joule* **3**, 1662–1676 (2019).
59. Fredericks, W. L., Sripad, S., Bower, G. C. & Viswanathan, V. Performance metrics required of next-generation batteries to electrify vertical takeoff and landing (VTOL) aircraft. *ACS Energy Lett.* **3**, 2989–2994 (2018).
60. Ko, Y. et al. Omics-enabled understanding of electric aircraft battery electrolytes. *Joule* **8**, 2393–2411 (2024).
61. Shen, X. et al. The failure of solid electrolyte interphase on Li metal anode: structural uniformity or mechanical strength? *Adv. Energy Mater.* **10**, 1903645 (2020).
62. Lin, Y. et al. Impact of the fluorination degree of ether-based electrolyte solvents on Li-metal battery performance. *J. Mater. Chem. A* **12**, 2986–2993 (2024).
63. Frisch, M. E. et al. Gaussian 16, Revision C.01 (Gaussian Inc., 2016).
64. Dennington, R., Keith, T. A. & Millam, J. M. GaussView v.6.0.16 (Semichem Inc., 2016).
65. Hanwell, M. D. et al. Avogadro: an advanced semantic chemical editor, visualization, and analysis platform. *J. Cheminform.* **4**, 17 (2012).
66. Bursch, M., Mewes, J. M., Hansen, A. & Grimme, S. Best-practice DFT protocols for basic molecular computational chemistry. *Angew. Chem. Int. Ed.* **61**, e202205735 (2022).
67. Zapata, J. C. & McKemmish, L. K. Computation of dipole moments: a recommendation on the choice of the basis set and the level of theory. *J. Phys. Chem. A* **124**, 7538–7548 (2020).
68. Jakalian, A., Bush, B. L., Jack, D. B. & Bayly, C. I. Fast, efficient generation of high-quality atomic charges. AM1-BCC model: I. *Methods J. Comput. Chem.* **21**, 132–146 (2000).
69. Humphrey, W., Dalke, A. & Schulten, K. VMD: visual molecular dynamics. *J. Mol. Graph.* **14**, 33–38 (1996).
70. Cohen, O. A. et al. SolvationAnalysis: a Python toolkit for understanding liquid solvation structure in classical molecular dynamics simulations. *J. Open Source Softw.* **8**, 5183 (2023).

71. Kim, S. C. et al. Potentiometric measurement to probe solvation energy and its correlation to lithium battery cyclability. *J. Am. Chem. Soc.* **143**, 10301–10308 (2021).
72. Bruce, P. G. & Vincent, C. A. Steady state current flow in solid binary electrolyte cells. *J. Electroanal. Chem. Interfacial Electrochem.* **225**, 1–17 (1987).

Acknowledgements

We acknowledge support from the Assistant Secretary for Energy Efficiency and Renewable Energy, Office of Vehicle Technologies of the US Department of Energy (DOE) under the Battery Materials Research (BMR) Program and Battery 500 Consortium. The cryo-TEM work was supported by the US DOE, Office of Basic Energy Sciences, Division of Materials Sciences and Engineering under contract DE-AC02-76SF00515. Part of this work was performed at the Stanford Nano Shared Facilities (SNSF), supported by the National Science Foundation under award ECCS-2026822. DFT calculations and MD simulations were conducted on the Sherlock cluster, operated by Stanford University and the Stanford Research Computing Center, to whom we would like to express our gratitude for their computational resources and support. I.R.C. acknowledges support from Stanford Graduate Fellowship (SGF) and SBS Foundation Fellowship for graduate studies at Stanford University. A.S. is grateful for support from the NSF Graduate Research Fellowship and SGF. S.C.K. acknowledges support from Stanford Energy Postdoctoral Fellowship.

Author contributions

I.R.C., Z.B. and Y. Cui conceived the idea. I.R.C. conducted the experiments and analysed the results under the guidance of Z.B., Y. Cui, and J.Q. I.R.C. performed synthesis, electrochemical measurements and materials characterization. Y. Chen carried out DOSY NMR. J.F. measured XPS measurements and GEIS. H.L. performed FIB-SEM and made UME. E.Z. performed H_2O titration techniques and viscosity measurements. C.S. conducted cryo-TEM. J.H. and A.S. carried out the DFT and MD simulations. J.H.L. conducted SEM images. Y.L. and I.R.C. synthesized and provided EME, MPE and FxEME. S.C.K. and I.R.C. measured solvation energies and entropy. H.P. measured ^{13}C, ^{19}F-NMR and heteronuclear single quantum coherence for solvents. P.Z., and J.L. provided technical help and helpful discussions. I.R.C., Y. Chen, A.S., J.Q., Y. Cui and Z.B. cowrote and revised the manuscript.

Competing interests

Z.B., Y. Cui and I.R.C. declare that this work has been filed as US Provisional Patent Application No. 63/689,564 and some molecules in this work have been included in previously filed International Application No. PCT/US2022/047472. A license related to PCT/US2022/047472 has been assigned to Feon Energy, Inc., in which Z.B. and I.R.C. owns equity. The remaining authors declare no competing interests.

Additional information

Supplementary information The online version contains supplementary material available at https://doi.org/10.1038/s41560-025-01716-w.

Correspondence and requests for materials should be addressed to Jian Qin, Yi Cui or Zhenan Bao.

Peer review information *Nature Energy* thanks Kai Liu and the other, anonymous, reviewer for their contribution to the peer review of this work.